Chinese Journal of
POLYMER SCIENCE

RESEARCH ARTICLE

https://doi.org/10.1007/s10118-026-3609-6
Chinese J. Polym. Sci. **2026**, *44*, 1883–1897

Polarity-regulated Nano-silica Steering Carbon Black Network Evolution and Reconfiguration in Conductive Silicone Elastomers: Experimental and Molecular Simulations

Bang-Wei Wan[a,b] and Yang Yang[a,b*]

[a] *Yunnan Key Laboratory of Disaster Reduction in Civil Engineering, Faculty of Civil Engineering and Mechanics, Kunming University of Science and Technology, Kunming 650500, China*
[b] *Yunnan International Joint Laboratory of Green Construction and Intelligent Maintenance, Faculty of Civil Engineering and Mechanics, Kunming University of Science and Technology, Kunming 650500, China*

Electronic Supplementary Information

Abstract Conductive elastomer composites (CEC) are widely used in flexible electronics, structural health monitoring, and aerospace applications. However, their resistive strain response often exhibits a shoulder peak effect, which undermines signal stability and measurement accuracy. In this study, the generation and suppression mechanisms of the shoulder peak effect were clarified by regulating hydrogen bonding interactions on the surface of nano-silica. Experimental results combined with molecular dynamics (MD) simulations demonstrate that in samples (OCV-260) fabricated with hydrophobic nano-silica (OB), the hydrophobic surface induces weak hydrogen bonding between conductive carbon black (CB) and OB. This interaction reduced the hysteresis area of the resistive-strain response by 78.84%, suppressed the adhesion-desorption migration of CB along silicone rubber (SR) molecular chains, and prevented sudden resistance spikes during unloading, thereby eliminating the shoulder peak effect. In addition, OCV-260 exhibited a 97.19% enhancement in the strain sensitivity coefficient (GF), a 53.20% extension of the monitoring range, and a rapid response time of 221 ms. Remarkably, no shoulder peak effect was detected, even after 1×10^4 loading-unloading cycles. These findings offer a promising strategy and broad application potential for achieving long-term, precise sensing in CEC for aerospace, flexible electronics, and structural health monitoring.

Keywords Conductive elastomer composites; Shoulder peak effect; Resistive-strain response signal; Hydrogen bonding; Nano-silica

Citation: Wan, B. W.; Yang, Y. Polarity-regulated nano-silica steering carbon black network evolution and reconfiguration in conductive silicone elastomers: experimental and molecular simulations. *Chinese J. Polym. Sci*. **2026**, *44*, 1883–1897.

INTRODUCTION

Conductive elastomer composites (CEC) are widely employed in aerospace, electronic skin, and structural health monitoring applications owing to their ability to generate resistivestrain response signals under deformation.[1–5] However, during practical monitoring, CEC frequently exhibits a shoulder peak effect,[6–10] characterized by abnormal inflection peaks in the Resistance-strain curve during unloading (Fig. S1 in the electronic supplementary information, ESI). This effect impairs the monitoring performance in three major ways: (1) it distorts the resistive-strain response, causing inaccuracies, irreversible resistance drift, and reduced signal stability; (2) in the long-term monitoring of large-scale engineering structures, particularly under significant deformation, it obscures real damage signals and elevates potential safety risks; and (3) under dynamic loading, it amplifies signal noise, thereby decreasing real-time response accuracy and monitoring reliability. To suppress the shoulder peak effect, various strategies have been proposed,[11–14] including designing tensile metamaterials with negative Poisson's ratios, introducing cationic/anionic surfactants to optimize conductive phase dispersion, fabricating serrated groove structures to minimize residual strain, and employing pre-stretching methods to regulate conductive network unloading. Although these approaches partially alleviate the problem, they generally require specialized equipment, involve complex chemical modifications, and incur high fabrication costs, limiting their practical applicability. Therefore, it is imperative to develop a simple and cost-effective fabrication strategy that can effectively suppress the shoulder peak effect.

In recent years, hydrogen bonding has emerged as an effective strategy to enhance the overall performance of elastomers. For example, Gao *et al.*[15] introduced a decuple hydrogen bonding design to construct a dynamic sacrificial hydrogen bond network, which imparted polydimethylsiloxane (PDMS) elastomers with excellent self-healing ability while markedly improving their strength and toughness. Wu *et al.*[16] developed a hierarchical sacrificial hydrogen-bond

* Corresponding author, E-mail: yangyang0416@kust.edu.cn
Received November 28, 2025; Accepted February 1, 2026; Published online May 14, 2026

network that enabled high strength, toughness, and self-healing in supramolecular polymers without the need for covalent crosslinking. Similarly, Liu *et al.*[17] enhanced the toughness and overall performance of polybenzoxazine coatings by regulating the sacrificial hydrogen bond networks within polyurethanes. Although sacrificial hydrogen bonds have been widely studied for improving the mechanical and self-healing properties of elastomers, their role in regulating the electromechanical response, particularly the shoulder peak effect, in conductive elastomers remains underexplored. Given the reversible and stress-responsive nature of hydrogen bonds, their impact on the dynamic reconfiguration of conductive networks and the stability of signal outputs are of critical importance for flexible sensing and strain monitoring. Moreover, molecular dynamics (MD) simulations[18,19] provide an effective means of probing material behavior at the atomic scale. By analyzing interatomic interactions and molecular motion, MD simulations enable the dynamic evaluation of hydrogen bond formation as well as the disruption and reconstruction of conductive networks, thereby offering theoretical support for elucidating the correlation between internal hydrogen bonding mechanisms and shoulder peak responses in CEC.

This study aims to eliminate the shoulder peak effect in CEC during strain monitoring to improve the stability and reliability of the resistive-strain response signals. Silicone rubber (SR) was selected as the elastomer matrix, and conductive carbon black (CB) as the conductive filler. Hydrophobic and hydrophilic nano-silica were introduced to regulate hydrogen bond formation by altering the surface polarity, thereby enabling the investigation of their influence on the resistive-strain response behavior of CEC, as shown in Fig. 1. By combining experimental approaches with molecular dynamics simulations, this study systematically elucidates the mechanism by which hydrogen bonding governs the generation and regulation of the shoulder peak effect. These findings provide new design strategies and theoretical guidance for CEC applications in aerospace, flexible electronics, and intelligent monitoring.

EXPERIMENTAL

Specific details regarding raw materials, preparation, characterization, *etc.*, are included in section **EXPERIMENTS AND SIMULATIONS** (in ESI).

RESULTS AND DISCUSSION

Formation and Elimination Mechanism of the CEC Shoulder Peak Effect

Figs. 2(a)–2(d) present the resistance-strain response signals of four conductive elastomer composites (CEC) at strain levels of 10%–50%. The signals of Hydrophilic Nano-Silica BET: 380 mg^2/g/CB-SR (ICV-380), hydrophilic nano-silica BET:260 mg^2/g/CB-SR (ICV-260), and hydrophilic nano-silica BET:150 mg^2/g/CB-SR (ICV-150) exhibited pronounced shoulder peak effects, severely compromising the reliability and stability of CEC monitoring. In contrast, the hydrophobic nano-silica BET:260 m^2/g/CB-SR (OCV-260) maintained a stable resistance-strain response relationship under all strain conditions. To elucidate the origin of the shoulder peak effect and its suppression, an analysis was conducted from the following perspectives.

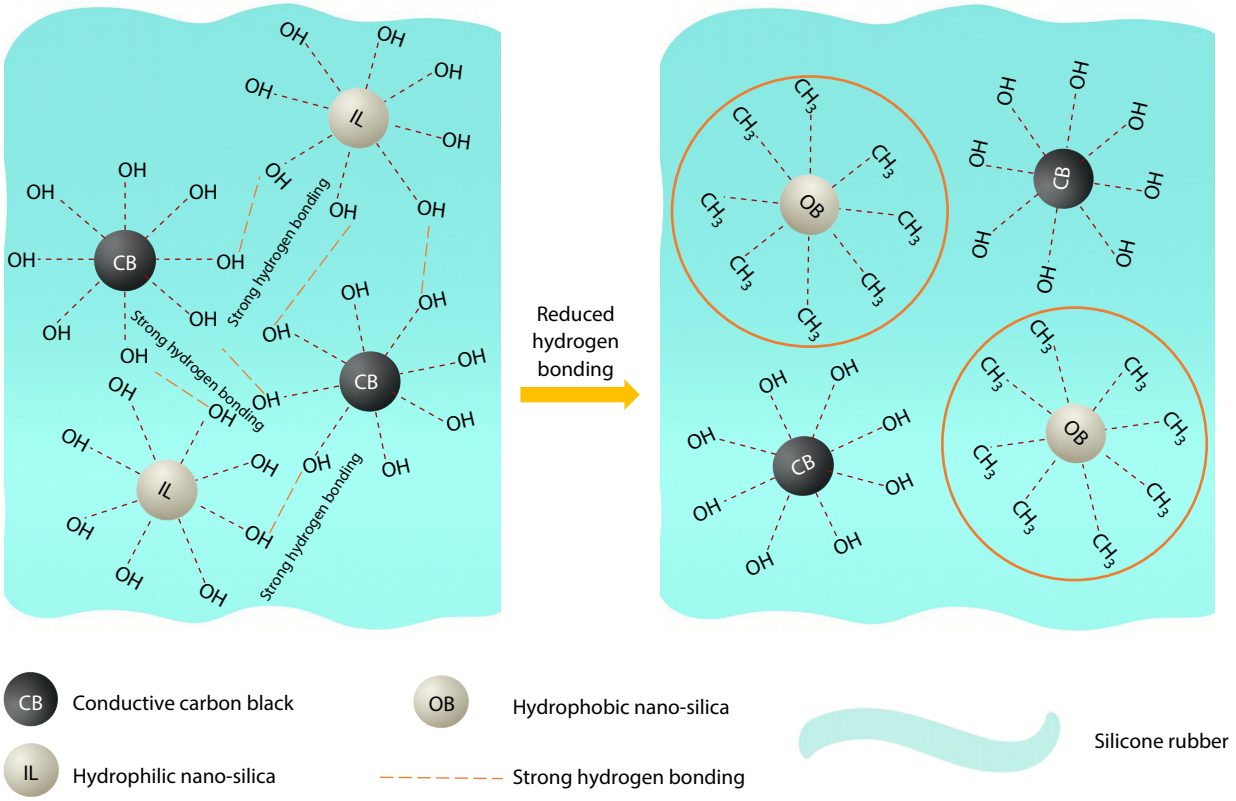

Fig. 1 Schematic of hydrogen bond regulation in conductive elastomers.

https://doi.org/10.1007/s10118-026-3609-6

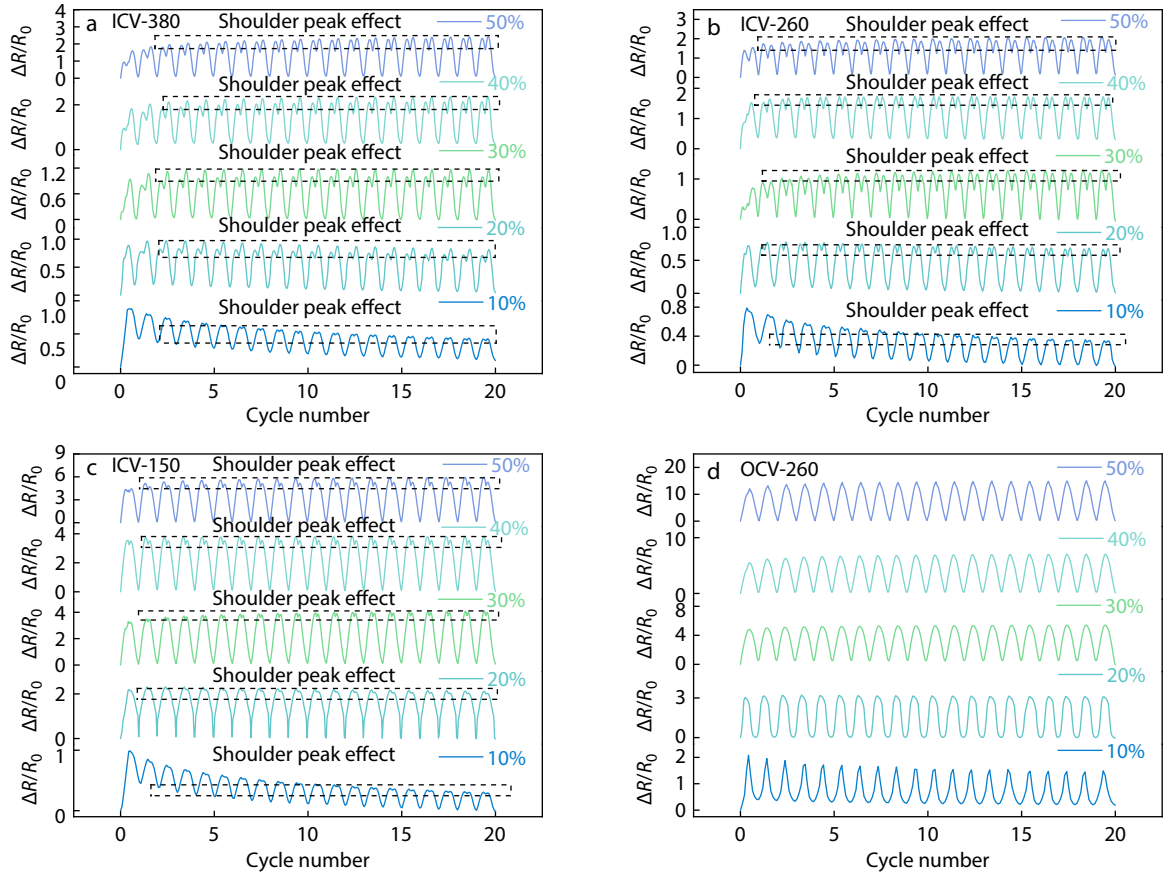

Fig. 2 (a) Resistance-strain response of ICV-380 at strain levels of 10%–50%; (b) Resistance-strain response of ICV-260 at strain levels of 10%–50%; (c) Resistance-strain response of ICV-150 at strain levels of 10%–50%; (d) Resistance-strain response of OCV-260 at strain levels of 10%–50%.

(1) Fig. S6 (in ESI) shows the FTIR spectra of IL-380, IL-260, IL-150, and OB-260. Characteristic absorptions of Si—OH and Si—O—Si appeared at 3400 and 1100 cm^{-1}, respectively. Baseline-corrected integration was performed in the 3600–3200 cm^{-1} region (hydrogen-bonded O—H broad band) and the 1200–1000 cm^{-1} region (Si—O—Si main band), and the normalized integral intensity ratio (HBI) was defined as the ratio of these two bands. A higher HBI indicates greater availability of effective sites for hydrogen bond formation.[20] The results show that OB-260 has a lower HBI than IL-380, IL-260, and IL-150, suggesting a weaker hydrogen bond formation capability as a filler within the matrix. Furthermore, Fig. 3(a) presents the FTIR spectra of the four CEC samples. Distinct absorption bands at 1403.86 and 1662 cm^{-1} are observed in the ICV series, corresponding to the symmetric stretching vibration of the carboxylate group ($-COO^-$) and the stretching vibration of the carbonyl group (C=O), respectively. The introduction of these polar groups significantly enhances the hydrogen bonding capacity and surface polarity, thereby improving hydrophilicity.[21,22] In contrast, the OCV-260 sample showed a markedly weaker $-COO^-$ peak and a complete absence of the C=O peak, leading to reduced surface polarity, weakened hydrogen bonding interactions, and diminished hydrophilicity.

XPS analysis was used to evaluate the influence of the hydroxyl (Si—OH) content on the hydrogen bond formation capability across the four CEC surfaces, as shown in Figs. 3(b)–3(e). The results show that the Si—OH binding energies are mainly distributed within the 532.3–532.6 eV range,[23,24] with the presence of Si—OH being essential for hydrogen bond formation. A comparison of the area ratio (AR) between Si and OH and Si—O—Si in each sample revealed the following order: ICV-380 > ICV-260 > ICV-150 > OCV-260. This indicates that ICV-380 has the highest density of polar surface groups and, therefore, the strongest hydrogen bonding capability. In contrast, OCV-260 exhibited the smallest Si—OH peak area and the narrowest peak width, reflecting the lowest surface polarity and the strongest hydrophobicity. Thus, the smaller AR of OCV-260 corresponds to weaker surface polarity and reduced hydrogen bonding capacity.

DMA testing was conducted to compare the storage modulus, loss modulus, and tanδ among the different CEC, reflecting the strength of their intermolecular interactions,[25,26] as shown in Figs. 3(f)–3(h). Among the ICV series, ICV-380 exhibited the highest storage modulus and the lowest tanδ peak, indicating the most restricted segmental motion and strongest intermolecular physical crosslinking. Its surface contains abundant Si—OH polar groups, which enable the formation of a dense hydrogen bond network between the matrix and conductive filler surface, thereby markedly enhancing the rigidity and cohesion of ICV-380. In contrast, OCV-260 showed the lowest modulus, highest tanδ, and right-shifted T_g, reflecting fewer surface polar groups, weaker hydrogen bonding, increased chain segment mobility, and stronger hy-

drophobicity.[25] Thus, the hydrogen bonding capacities of the four CEC decreased in the following order: ICV-380 > ICV-260 > ICV-150 > OCV-260. These results further demonstrate that the type and content of surface polar groups are critical factors in regulating the hydrogen bond network and overall performance of the CEC.

AFM adhesion force testing was conducted to examine the relationship between the differences in surface polarity among the four CEC types and their hydrogen bond formation capabilities,[27,28] as shown in Figs. 3(i)–3(l). The adhesion force plots and corresponding average values are presented in Figs. 3(i)–3(l) and Table S1 (in ESI). ICV-380 showed the highest average adhesion force (18.30 nN), followed by ICV-260 (17.80 nN), ICV-150 (16.10 nN), and OCV-260 exhibited the lowest value (15.50 nN). Stronger adhesion generally indicates stronger interactions between the Si and OH groups and the probe, indirectly reflecting the enhanced hydrogen-bonding capacity. These results demonstrate that the ICV series has a significantly higher surface polarity than hydrophobic-modified OCV-260, providing more active sites for hydrogen bond formation. In contrast, the hydrophobic nature of OCV-260 reduced the number of polar groups and weakened adhesion, resulting in the lowest hydrogen bonding capacity.

Water contact angle (WCA) testing was performed to com-

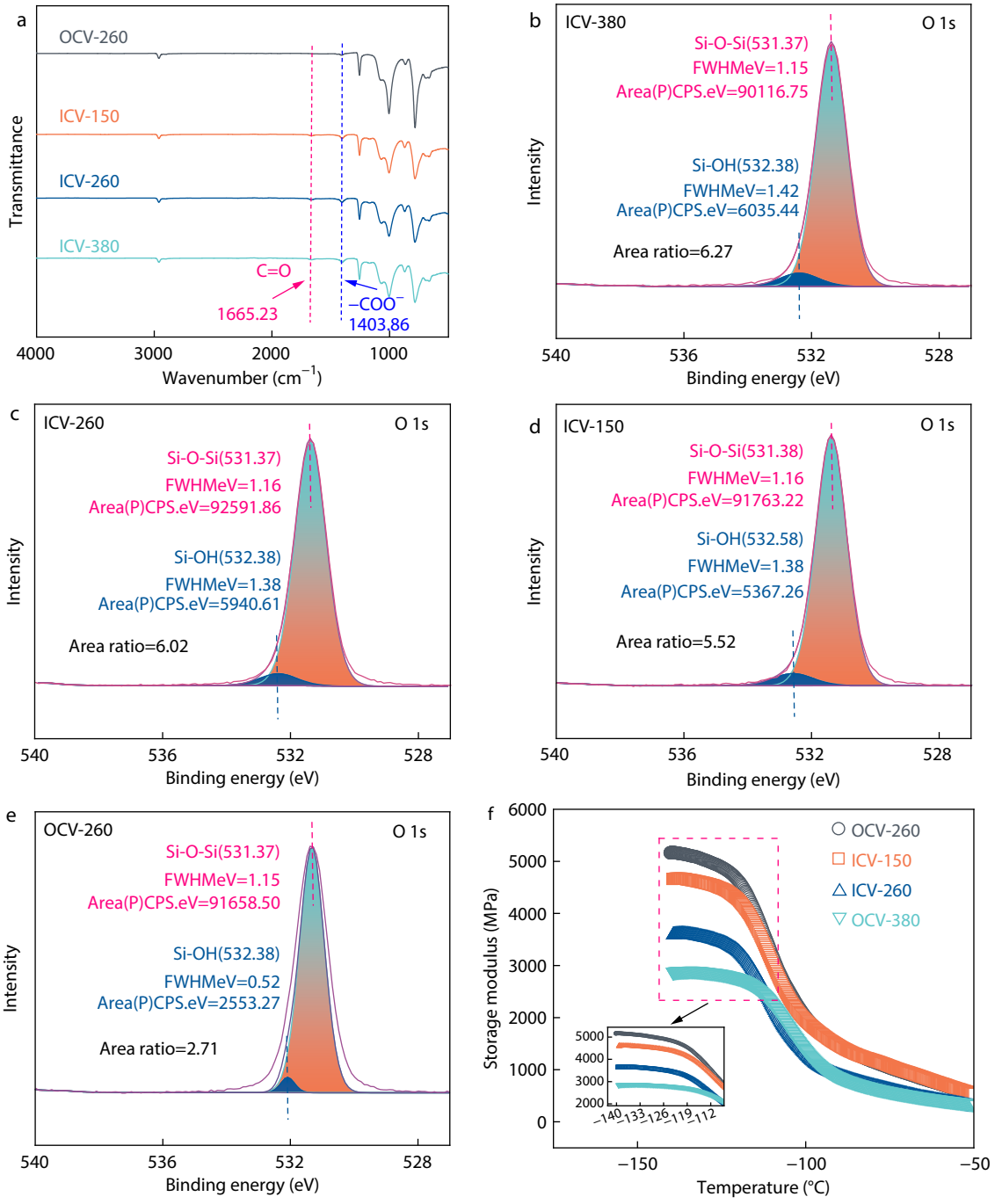

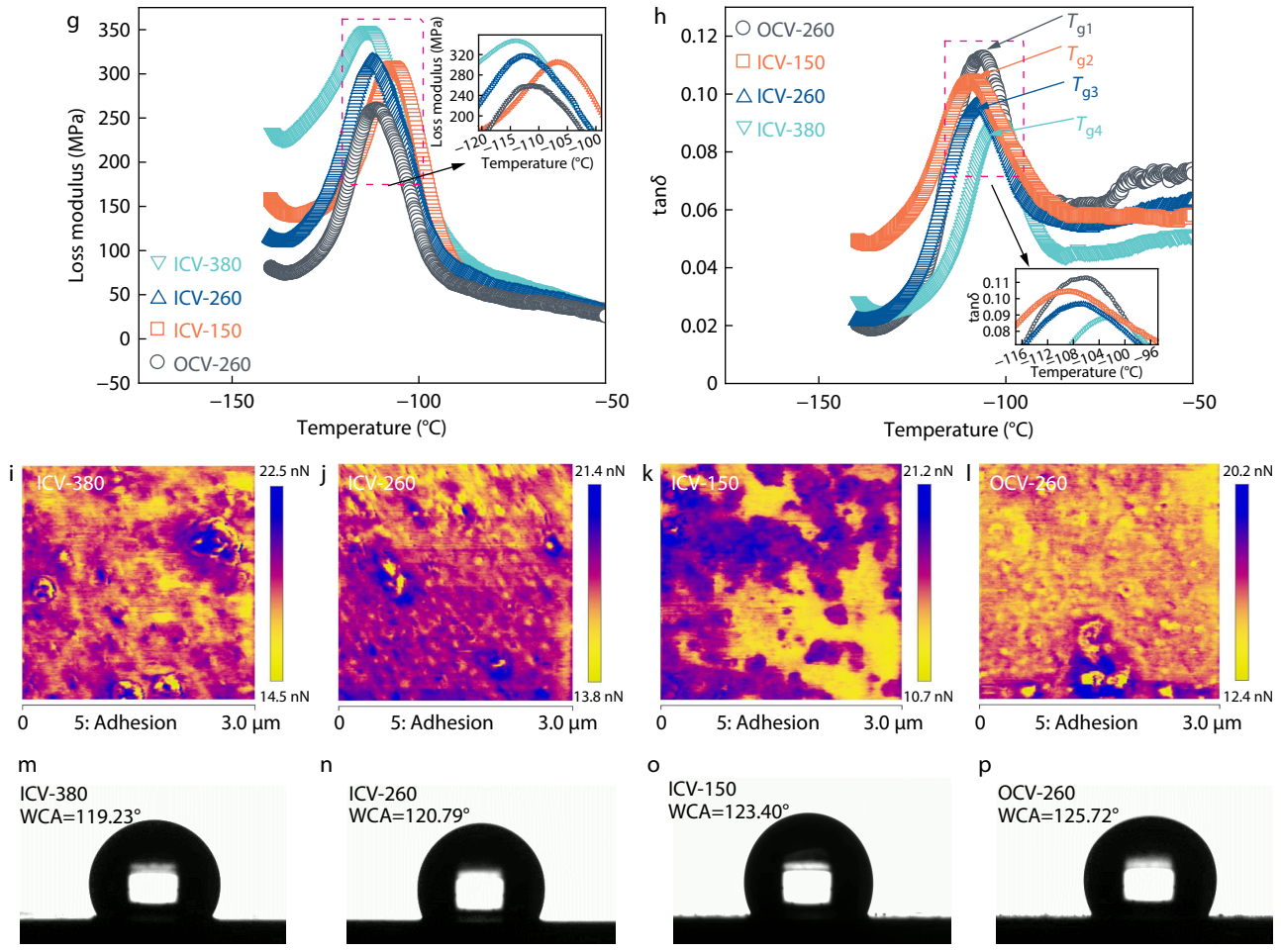

Fig. 3 (a) FTIR spectra of OB-260, IL-150, IL-300, and IL-380; (b–e) XPS spectra of the four CEC; (f–h) DMA results of the four CEC; (i–l) Adhesion force plots of the four CEC; (m–p) Contact angle plots of the four CEC.

pare the surface polarities of the four CEC samples, indirectly reflecting their hydrogen bond formation capabilities,[29,30] as shown in Figs. 3(m)–3(p). Smaller contact angles indicate stronger surface polarity and greater hydrogen-bonding capacity. The measured contact angles of ICV-380, ICV-260, and ICV-150 were 119.23°, 120.79°, and 123.40°, respectively, which were lower than the 125.72° observed for OCV-260. This demonstrates that the ICV series surfaces are more hydrophilic, with higher Si—OH exposure and a stronger ability to form hydrogen bonds with the substrate or water molecules. In contrast, the hydrophobic nature of OCV-260 reduces Si—OH exposure, producing a more hydrophobic surface and weaker hydrogen-bonding interactions.

The shoulder peak effect primarily originates from differences in the interfacial interaction strength between conductive carbon black (CB) and nano-silica, combined with the reconfigurable nature of the conductive network. Hydrophilic silica surfaces, enriched with Si—OH groups, formed extensive hydrogen bonds with Si—OH groups on the CB surfaces. This strong interfacial bonding restricts the free slip of the CB particles and induces dynamic adhesion-desorption behavior during strain loading. As a result, the conductive pathways are frequently broken and reconstructed, leading to nonlinear, reversible, and unstable resistance responses, which are typical shoulder effect peaks. In contrast, hydrophobic silica has lower surface polarity and weaker hydrogen bonding, allowing CB particles to slide more freely. This maintains the continuity and stability of the conductive network under strain, producing a linear and stable Resistance-strain response signal.

(2) The 10th resistance-response cycle at 40% strain was selected for each of the four CEC, as shown in Figs. 4(a)–4(d). For ICV-380, ICV-260, and ICV-150, the resistance increased with strain during tensile loading (AB) and decreased during unloading (BC). Owing to the viscoelastic hysteresis of SR, the resistance then increased sharply (CD), producing a shoulder peak effect, as shown in Figs. 4(a)–4(c). In contrast, the OCV-260 maintained a monotonic linear resistance response during loading and unloading. No sudden increase in resistance occurred during unloading, and no shoulder peak effect was observed. Thus, the second cause of the shoulder peak effect is the competition between the conductive network reconstruction and the SR viscoelasticity. The hysteresis areas of the resistance-response signals for the four composites were calculated using $A_H = \frac{|A_S - A_R|}{A_S}$, where A_S,A_R represent the areas under the tensile and unloading curves, respectively. A_{H1}, A_{H2}, A_{H3}, and A_{H4}correspond to hysteresis areas of ICV-380,

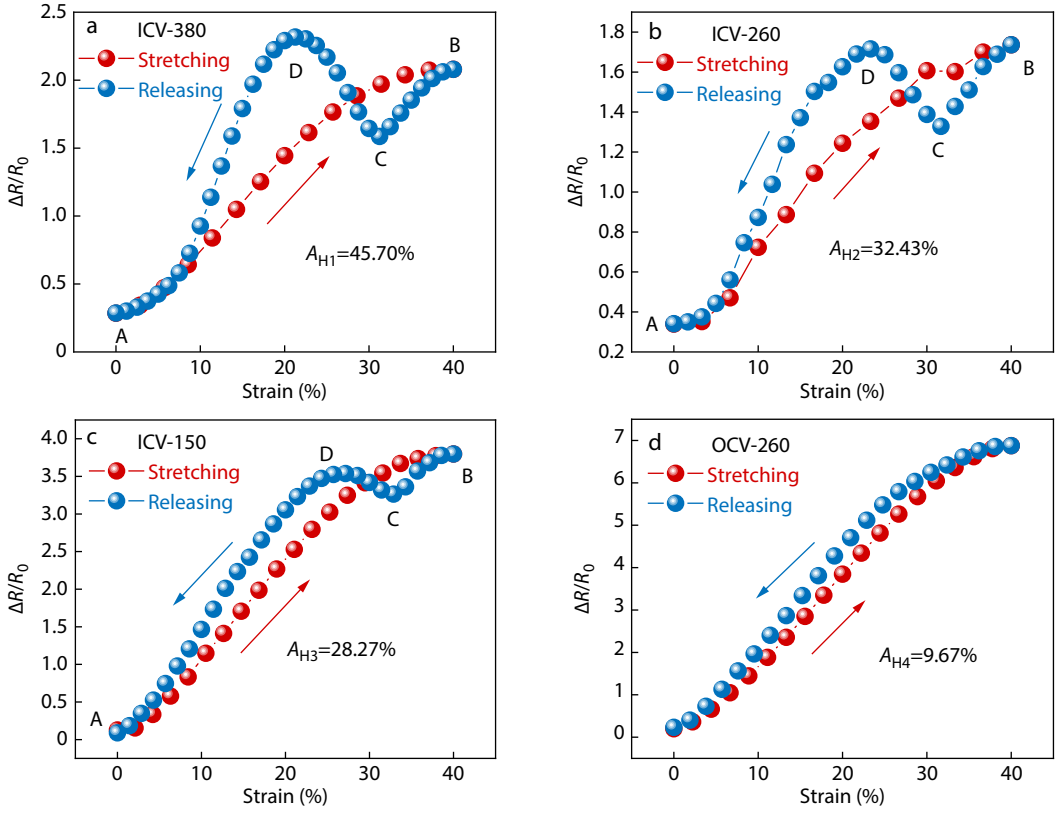

Fig. 4 (a) 10th tensile-unloading cycle at 40% strain for ICV-380; (b) 10th tensile-unloading cycle at 40% strain for ICV-260; (c) 10th tensile-unloading cycle at 40% strain for ICV-150; (d) 10th tensile-unloading cycle at 40% strain for OCV-260.

ICV-260, ICV-150, and OCV-260, respectively. A larger A_H indicates poorer recovery of the resistance–response signal. As shown in Figs. 4(a)–4(d), the hysteresis areas were A_{H1}=45.70%, A_{H2}=32.43%, A_{H3}=28.27%, and A_{H4}=9.67%, representing a 78.84% reduction. This demonstrates the excellent recovery performance of the OCV-260 Resistance-strain response signal.

(3) Dispersion performance of CEC. Figs. 5(a)–5(d) show the SEM images of the four CEC. In the ICV-380 and ICV-260 samples, CB particles were extensively adsorbed on the surfaces of IL-380 and IL-260. This is because the surfaces of IL-380 and IL-260 are rich in Si—OH groups, which readily form hydrogen bonds with the —OH groups on the CB surface. As a result, CB aggregates around the IL-380 and IL-260 particles, disrupting the continuous distribution of CB in the SR, as shown in Figs. 5(a) and 5(b). During strain unloading, the conductive pathways underwent severe restructuring and disconnection, leading to a pronounced shoulder peak in the Resistance-strain response signal. In contrast, ICV-150 exhibited significantly reduced adsorption between the CB particles and IL-150 because of the lower content of hydrogen-bonding groups on the IL-150 surface. This effect is even more evident in OCV-260, where the SEM image clearly shows that the CB particles are not adsorbed onto the OB-260 surface. Because of the surface hydrophobicity, a volume exclusion effect occurs, maintaining good spatial separation between the CB particles and OB-260. This repulsive effect effectively suppressed CB agglomeration and preserved the structural stability of the conductive network during strain. Consequently, OCV-260 maintained continuous and controllable conductive pathways throughout loading and unloading, thereby eliminating the shoulder peak effect. This microstructural evidence demonstrates that regulating the surface hydrogen bonding capacity not only affects the interfacial bonding strength, but also governs the formation of conductive pathways and response stability.

Additionally, the microstructures of the four CEC were analyzed using RPA and AFM. Figs. 6(a)–6(c) show the storage modulus (G'), loss factor (tanδ), and complex viscosity (η^*) of the four CEC at 100% strain. As shown in Fig. 6(a), the G' values of all samples decreased with increasing strain owing to disruption of the conductive network within the CEC, a phenomenon known as the Payne effect.[31] This effect was used to evaluate the dispersion of the conductive fillers in the matrix,[32] with $\Delta G' = \Delta G'_{9.98\%} - \Delta G'_{99.98\%}$ as the evaluation criterion. Here, $\Delta G'$ represents the difference between G' at the maximum and minimum strains, whereas $\Delta G'_{9.98\%}$ and $\Delta G'_{99.98\%}$ correspond to G' values of 9.98% and 99.98% strain, respectively. A smaller $\Delta G'$ indicates a weaker Payne effect, better filler dispersion, and more stable conductive network. Calculations from Fig. 6(a) yield G' values of 59.55, 49.40, 42.17, and 36.75 kPa for the four CEC, representing a 38.28% reduction and confirming the excellent dispersion of CB in OCV-260. Fig. 6(b) shows the tanδ curves of the four samples. Lower tanδ values typically reflect more uniform filler dispersion in the elastomer matrix and a more stable interfacial structure. OCV-260 exhibited a significantly lower tanδ than the other three samples, indicating fewer internal hydrogen bonds, reduced polar interactions, and a more uniform CB

https://doi.org/10.1007/s10118-026-3609-6

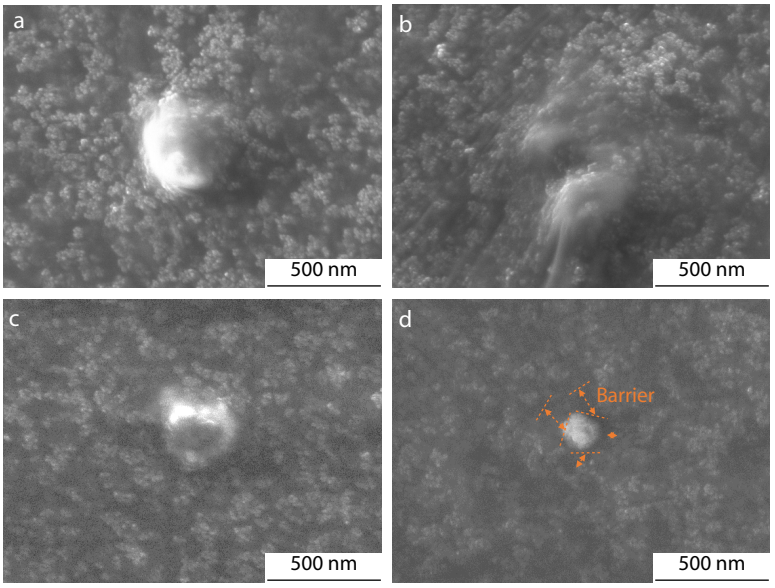

Fig. 5 SEM images of (a) ICV-380, (b) ICV-260, (c) ICV-150, and (d) OCV-260, respectively.

distribution within the SR matrix, thereby improving the structural integrity of the conductive network. Fig. 6(c) presents the complex viscosity (η^*) of the four CEC at 100% strain. This parameter reflects molecular chain entanglement and filler distribution uniformity under dynamic shear.[33] Lower η^* values indicated better flowability during processing, more uniform filler dispersion, and lower viscous resistance. OCV-260 exhibited the lowest η^*, which was significantly lower than those of ICV-380, ICV-260, and ICV-150, demonstrating its superior flow characteristics and filler dispersion during compounding. This is attributed to the lower surface polarity of IL-260 in OCV-260, which minimizes the strong hydrogen bonding interactions with CB. Consequently, the interfacial adhesion energy is reduced, CB adsorption and retention under high shear are decreased, and agglomeration during processing is prevented, leading to uniform dispersion and lower viscous resistance. In contrast, the ICV series, particularly ICV-380 and ICV-260, exhibited strong hydrophilicity. Their surfaces, which are rich in Si—OH groups from IL-380 and IL-300, readily form extensive hydrogen-bond networks with CB. While this strengthens the interfacial bonding and rigidity, it also induces excessive structuring of the filler network under dynamic shear, increasing hysteresis, reducing flowability, and increasing η^*. In summary, the lower η^* of OCV-260 not only highlights its superior dispersion capability during processing, but also reflects a more moderate spatial arrangement and greater structural flexibility of its conductive fillers.

Figs. 6(d)–6(k) show the microscopic surface morphology and three-dimensional contour maps of the four CEC samples, further illustrating the regulatory effect of the fillers on the SR structure. As observed in the two-dimensional and three-dimensional AFM images (Figs. 6d–6k), the OCV-260 sample exhibited a relatively smooth surface with minimal undulation. In contrast, the ICV-150, ICV-260, and ICV-380 samples displayed distinct undulating structures with uneven surfaces, indicating a higher micro-roughness. Further analysis of the average surface roughness (R_a) and root-mean-square roughness (R_q) values in Fig. 6(l) shows that OCV-260 had the lowest R_a and R_q, confirming its superior surface flatness, specific data are provided in Table S1 (in ESI). This flatness promotes uniform CB distribution within the SR matrix and enhances the continuity of the conductive network. A flatter interface reduces CB aggregation and improves free mobility, enabling the formation of more uniform, stable, and reconfigurable conductive pathways. In contrast, the ICV series exhibited higher surface roughness owing to the abundance of Si—OH groups on the IL-380, IL-300, and IL-150 surfaces. While these groups form hydrogen bonds with CB, they also introduce excessive interfacial adhesion points during the composite formation. This promotes CB enrichment in localized regions, leading to adhesion-desorption structures and pronounced surface undulation. Such rough microstructures not only reduce the controllability of the filler distribution, but also weaken the stability of conductive pathways, increase interfacial energy dissipation, and induce nonlinear resistance responses.

(4) Molecular dynamics simulation. To further investigate the influence of hydrogen bonds on the CEC shoulder effect peak, molecular dynamics (MD) simulations were performed. Figs. 7(a)–7(f) show the mean square displacement (MSD), radial distribution function (RDF), radius of gyration (ROF), free volume fraction (FFV), and hydrogen bond counts during the CEC pulling simulation. The MSD reflects the restriction of interfacial chain motion within the matrix, with higher values indicating weaker confinement by hydrogen bond interactions (S2.2.5).[34] As shown in Fig. 7(a), OCV-260 exhibits the highest MSD trend, indicating the weakest hydrogen bond formation capability. RDF evaluates hydrogen bond formation within the hydrogen bond shell (approximately 1.5–2.6 Å), where higher values represent stronger interfacial hydrogen bonding interactions (S2.2.6).[35] As shown in Fig. 7(b), OCV-260 shows the lowest RDF, and the magnified view in the 1.5–2.6 Å range confirms weaker hydrogen bonding compared with the other three CEC. ROF measures the compaction and adhesion of CB chains at the interface, where smaller values indicate tighter chain packing and stronger confinement owing to hydrogen bonding (S2.2.7).[36] As

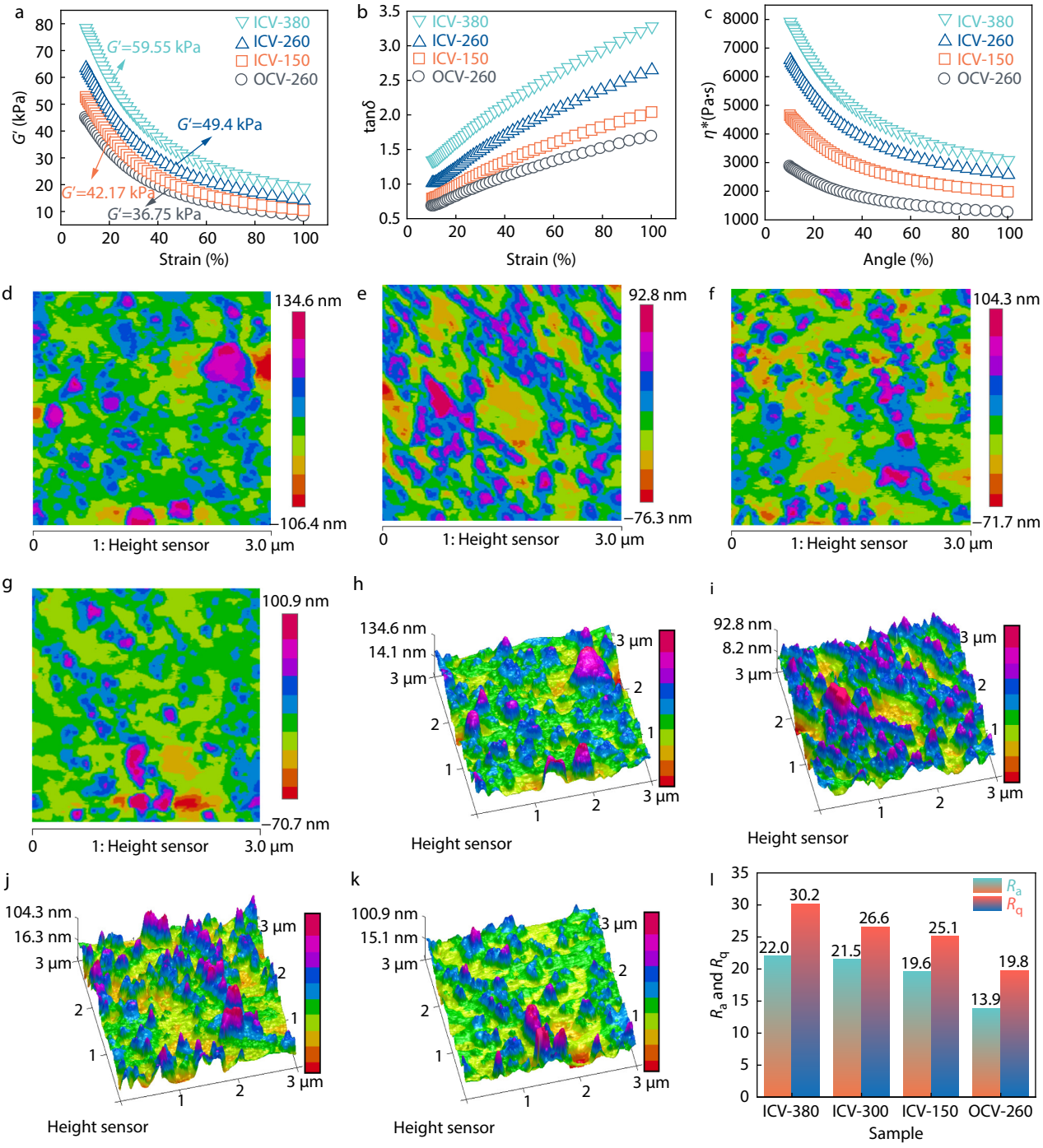

Fig. 6 (a–c) RPA of four CEC types; (d–g) AFM micrographs of four CEC types; (h–k) 3D hub images from AFM of four CEC types; (l) R_a versus R_q statistical plot for four CEC types.

shown in Fig. 7(c), OCV-260 consistently exhibits the highest ROF, reflecting the weakest interfacial densification and segment confinement. FFV evaluates the densification and porosity of the interfacial layer, with higher values corresponding to greater free volume, looser segments, and weaker hydrogen-bonding capacity (S2.2.8).[37] OCV-260 showed the highest FFV, which increased by 56.66%, confirming its weaker hydrogen-bonding capacity. The hydrogen bond formation during the peeling simulation was also analyzed at 1, 50, 150, 200, and 250 Ps, as shown in Figs. 7(e) and 7(f) and Figs. S7–S9 (in ESI). OCV-260 consistently formed fewer hydrogen bonds than the other three CEC, further indicating its weaker hydrogen-bonding capability. These computational findings were consistent with the experimental results.

Therefore, experiments consistent with molecular dynamics (MD) simulations indicate that the emergence or suppression of the shoulder peak effect is not determined by a single structural phenomenon in isolation but rather results from network restructuring driven by the strength of interfacial interactions coupled with the viscoelasticity of the matrix. The

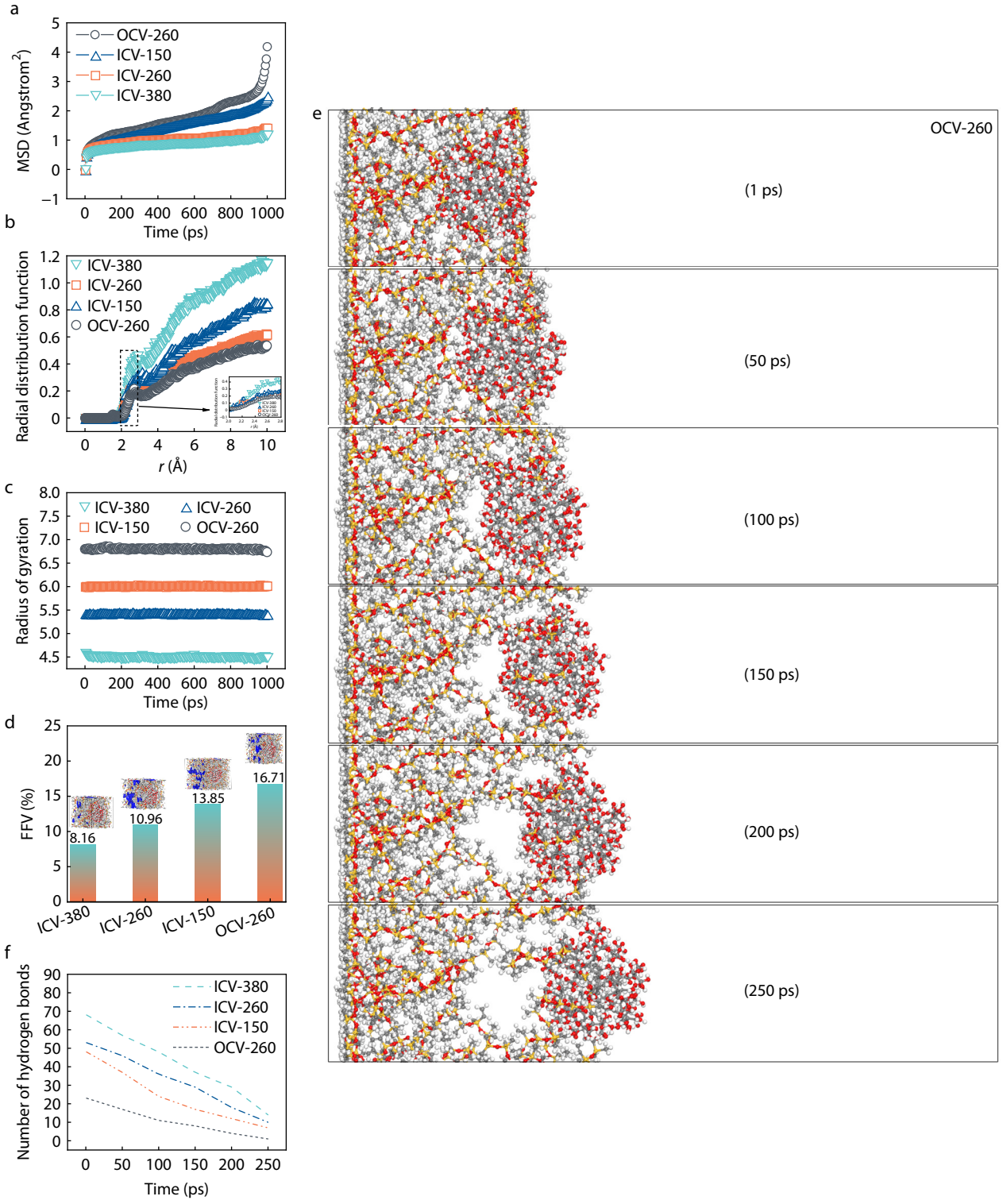

Fig. 7 (a) MSD of the four CECs; (b) RDF of the four CECs; (c) ROF of the four CECs; (d) FFV of the four CECs; (e) Peeling simulation process of OCV-260; (f) Evolution of hydrogen-bond formation during the peeling simulation for the four CECs.

hydrogen bonds discussed in this paper can be categorized into three types of interfacial interactions: CB-SiO_2, SiO_2-CB/SR, and CB-SR. Among these, the SiO_2–CB/SR interfacial hydrogen bonds play a dominant role in suppressing the shoulder peak effect. This is because the abrupt restructuring of the conductive pathways during the unloading phase is primarily triggered by the anchoring–release–re-anchoring (adhesion-desorption migration) of the conductive phase CB at the interface. Furthermore, SiO_2–CB and CB–SR interactions primarily modulate segment motion and viscoelastic

https://doi.org/10.1007/s10118-026-3609-6

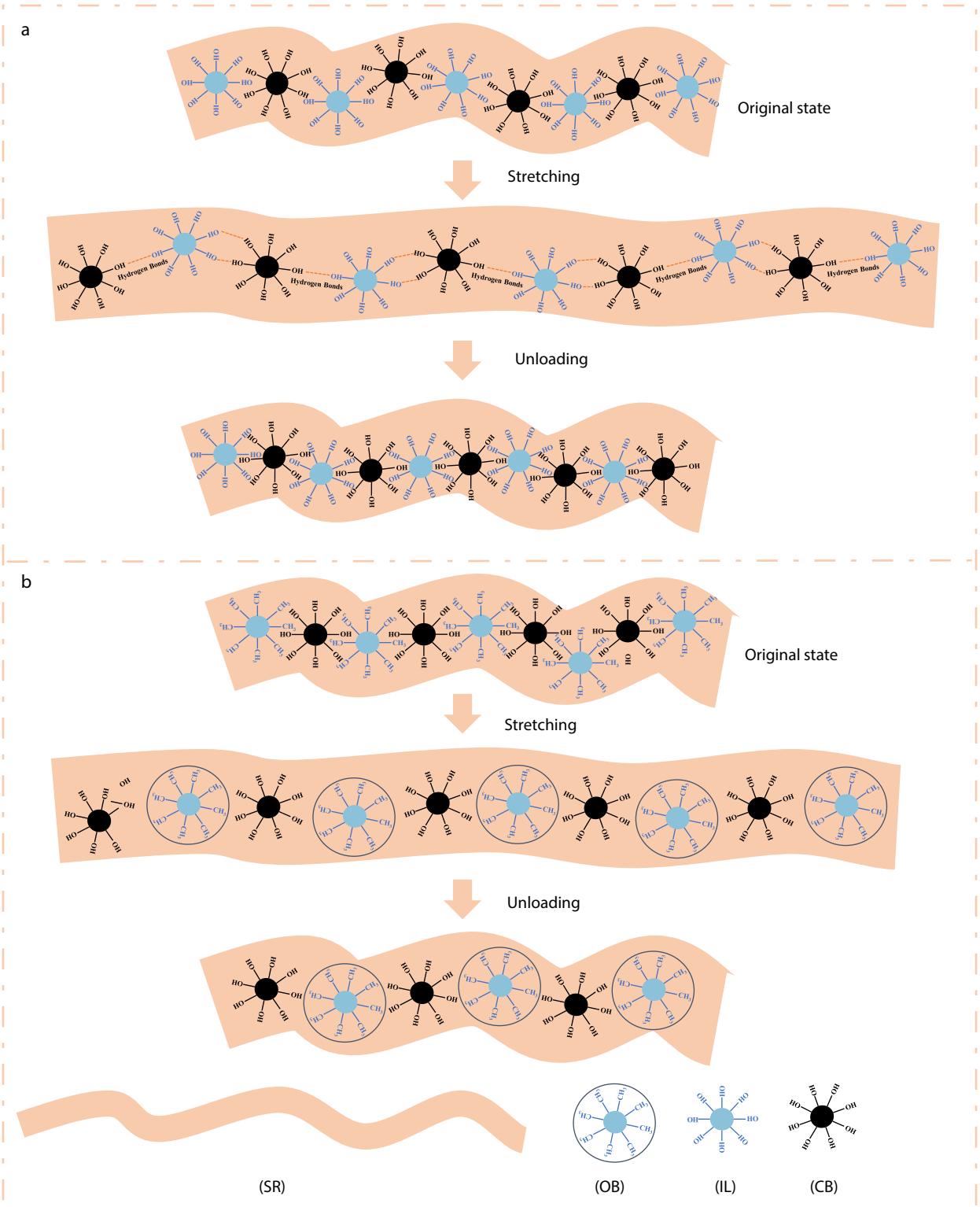

Fig. 8 (a) Schematic diagram of mutual contact between CB and IL within the SR during the tension-unloading process in CEC; (b) Schematic diagram of mutual contact between CB and OB within the SR during the tension-unloading process in CEC.

timing, potentially influencing response hysteresis, but not constituting the primary interface governing shoulder peak emergence or suppression. Thus, inhibiting the CB-SiO_2/SR interfacial hydrogen bonding is crucial for achieving a stable linear resistance response and eliminating the shoulder peak effect.

https://doi.org/10.1007/s10118-026-3609-6

When hydrophilic silica surfaces are rich in Si—OH groups, the CB-SiO_2/SR hydrogen bonds are strong, and interface anchoring is pronounced. During loading-unloading cycles, adhesion-desorption migration readily occurs, inducing frequent pathway breakage and reconstruction. Combined with the viscoelastic hysteresis of SR, the unloading phase is more prone to sudden resistance increases and larger hysteresis areas, which is known as the shoulder peak effect. Conversely, OB-260 reduces the surface polarity of SiO_2 and Si—OH exposure through hydrophobic modification, significantly weakening CB-SiO_2/SR hydrogen bonding. weakening the interfacial anchoring while preserving the steric effects and a uniform spatial distribution. This facilitates CB slip and enables conductive pathways to evolve through continuous rearrangement rather than abrupt reconstruction, thereby avoiding resistance spikes during unloading and eliminating the shoulder effect (Figs. 8a and 8b).

Force-Electric Response Performance Of CEC

Figs. 9(a) and 9(b) illustrate the mechanical properties of the four CEC formulations. Statistical analysis of stress-strain curves, tensile strength, and elongation at break showed that ICV-380 exhibited significantly higher tensile strength (4.58 MPa) and elongation at break (838.88%) than ICV-260, ICV-150, and OCV-260, indicating superior rigidity and ductility. AFM modulus mapping further reveals average moduli of 2.16 MPa and 2.14 MPa for ICV-380 and ICV-260, respectively, both much higher than ICV-150 (1.36 MPa) and OCV-260 (1.83 MPa), as shown in

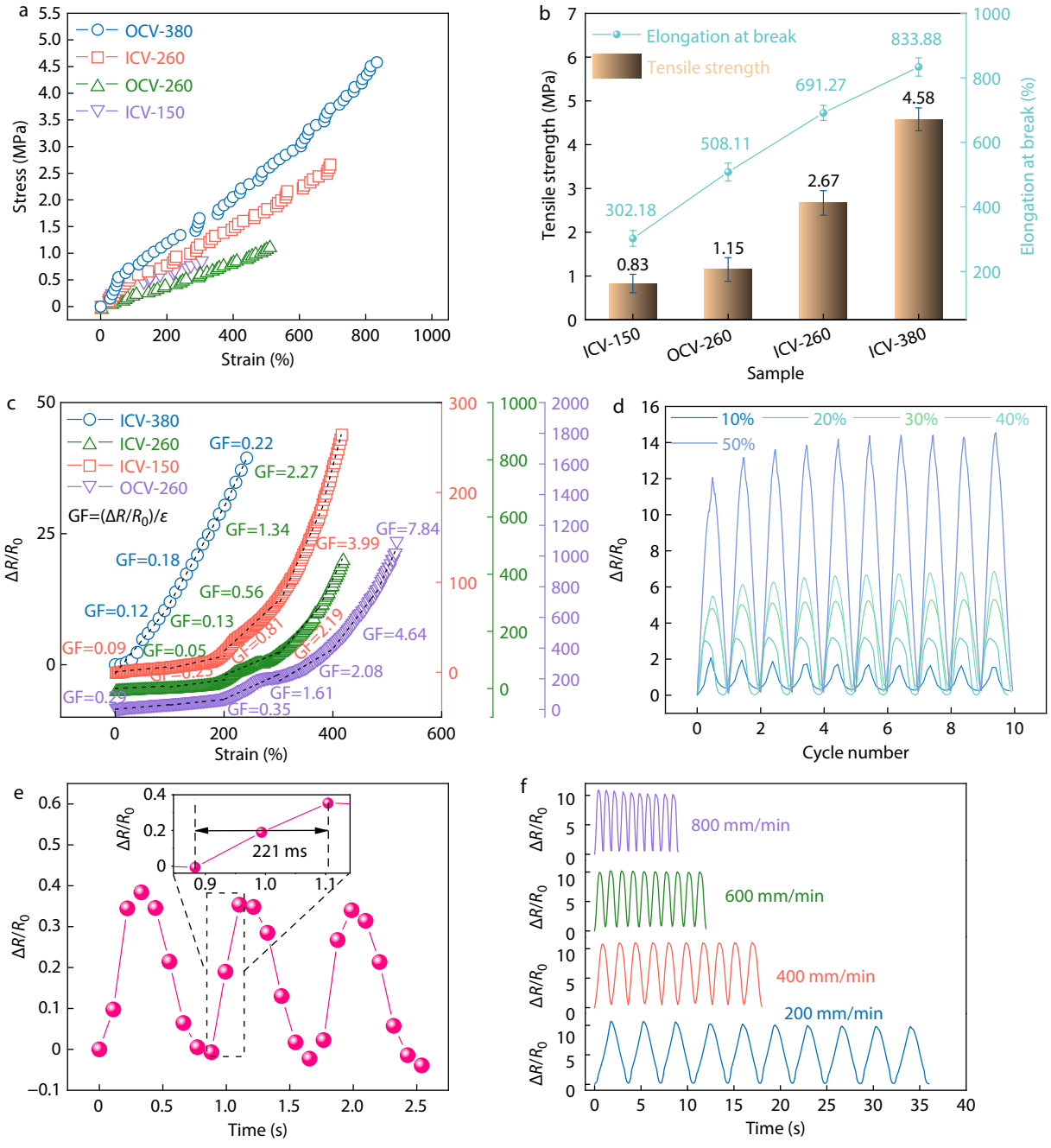

https://doi.org/10.1007/s10118-026-3609-6

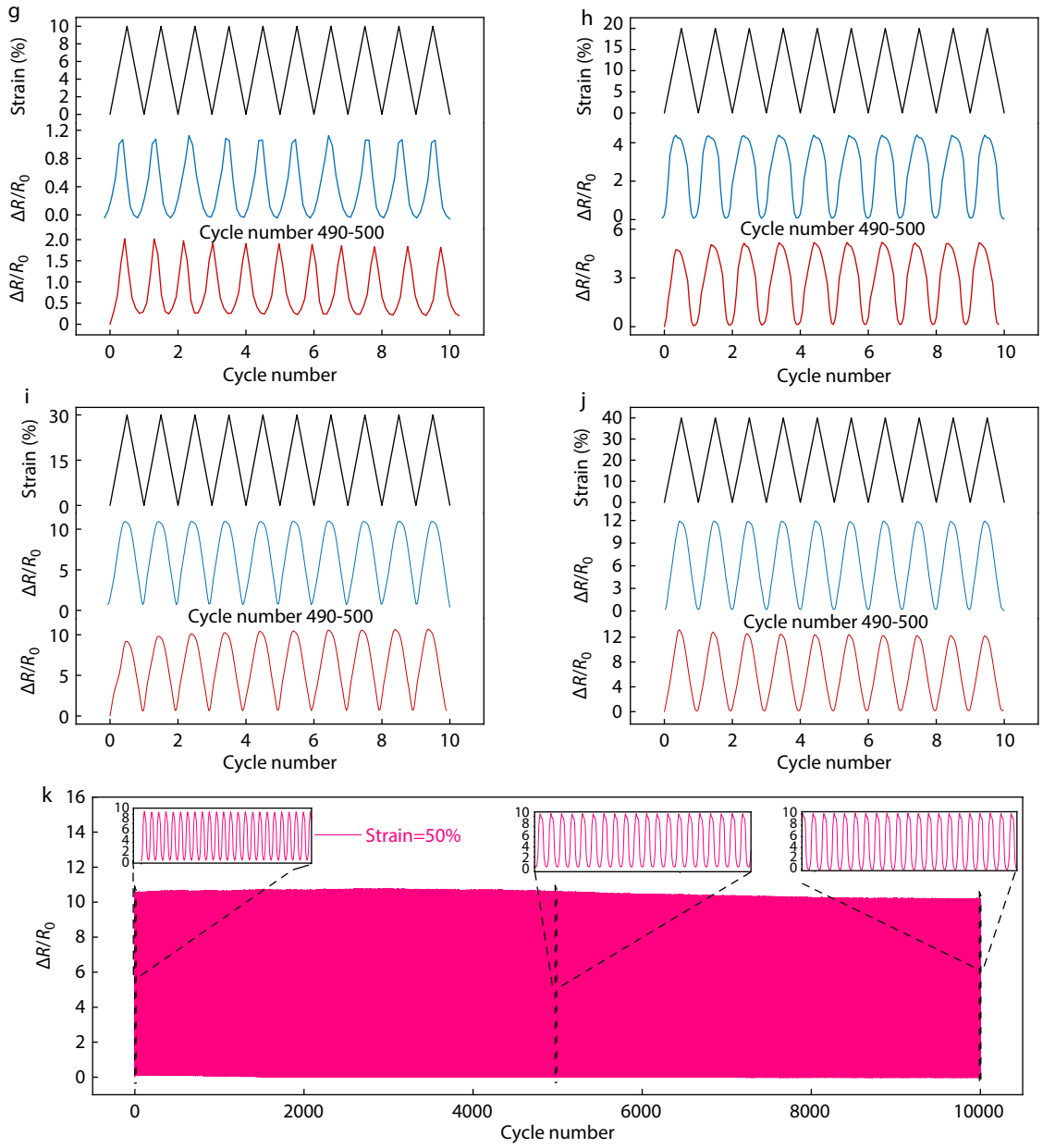

Fig. 9 (a) Strain-strain curves for the four CEC types; (b) Statistical plot of tensile strength and elongation at break for four CEC types; (c) Uniaxial resistance/strain response plots for four CEC types; (d) Resistance-strain response signal plots for OCV-260 at different strains; (e) Recovery time of resistance-strain response signal for OCV-260 at 1% strain and 1000 mm/min strain rate; (f) OCV-260 resistance response signature at different strain rates; (g–j) OCV-260 resistance-strain response signature after 500 cycles at 10%, 20%, 30%, and 40% strain; (k) OCV-260 resistance-strain response signature after 1×10^4 cycles at 50% strain.

Fig. S10 and Table S2 (in ESI). This enhancement was attributed to the use of hydrophilic nano-silica with a high specific surface area in the ICV series, particularly ICV-380. Its surface is enriched with polar Si—OH groups, enabling the formation of a dense hydrogen bond network with CB, which strengthens the interfacial bonding and increases the modulus and stress-bearing capacity. In contrast, OCV-260 employs surface-hydrophobized nano-silica with reduced polarity and significantly fewer Si—OH groups, resulting in weak hydrogen bonding and, consequently, lower modulus and strength. The cyclic hysteresis curves (Fig. S11 in ESI) further demonstrated the influence of the reversible adhesion–desorption mechanism of hydrogen bonds on the dynamic response. The energy dissipation during loading–unloading is characterized by the hysteresis area coefficient $H_R = \frac{L - L_R}{L}$, where L is the tensile area and L_R is the unloading area. ICV-380 and ICV-260 exhibited pronounced hysteresis and substantial energy dissipation (H_R=18.99% and 18.63%, respectively), indicating that hydrogen bond-induced structural rearrangement drives nonlinear mechanical responses and contributes to the shoulder peak effect. In contrast, OCV-260, despite using hydrophobic nano-silica with low surface polarity and lacking hydrogen bond support, shows a relatively stable conductive network. Although it had a lower modulus (1.83

MPa) and tensile strength (1.15 MPa), it exhibited the smallest hysteresis area H_R=14.28%). Weak hydrogen bonding reduces interfacial adhesion, resulting in loose CB contacts, greater filler migration, and frequent pathway breakage and reconstruction, which conversely lowers stress hysteresis. Fig. 9(c) shows the Resistance-strain responses of the four CEC under uniaxial loading. Resistance increased with strain in all cases, but OCV-260 exhibited a 96.33% higher strain sensitivity than ICV-380, highlighting its superior responsiveness for real-time monitoring. Sensitivity was evaluated using GF = $(\Delta R/R_0)/\varepsilon$, where $\Delta R = R - R_0$, R_0 is the initial resistance, R is the measured resistance, and ε is the strain. Linear fitting yielded maximum GF values of 0.22, 2.27, 3.99, and 7.84 for ICV-380, ICV-260, ICV-150, and OCV-260, respectively. OCV-260 showed a 97.19% increase in GF and a 53.20% expansion in the monitoring range, confirming a broader sensing range and higher sensitivity. Fig. 9(d) shows the stable resistance response of OCV-260 across various strains. As shown in Fig. 9(e), OCV-260 exhibits a response time of 221 ms at 1% strain and a rate of 1000 mm/min, faster than the other CEC.[38–43] Fig. 9(f) shows the resistance response signals of OCV-260 at different strain rates, indicating that the Resistance-strain response is unaffected by the strain rate. Figs. 9(g)–9(j) and Fig. S12 (in ESI) shows the dynamic resistance response signals of OCV-260 after 500 cycles at strain levels of 10%, 20%, 30%, and 40%. As shown in Figs. 9(g)–9(j), no shoulder peak effect was observed in the resistance response signals from either the first 10 cycles or the last 10 cycles. To further evaluate the stability, a 1×10^4-cycle resistance response test was conducted at 50% strain, as shown in Fig. 9(k). The magnified section confirms that no shoulder peak effect occurs throughout the entire 1×10^4-cycle tensile-unloading process. These results demonstrate that the conductive network structure of OCV-260 possesses an excellent damagereconstruction capability.

CONCLUSIONS

In this study, hydrogen bond-regulated conductive elastomers (CEC: ICV-380, ICV-260, ICV-150, and OCV-260 Hydrophilic Nano-Silica BET: 380 mg^2/g/CB-SR (ICV-380), hydrophilic nano-silica BET:260 mg^2/g/CB-SR (ICV-260), hydrophilic nano-silica BET:150 mg^2/g/CB-SR (ICV-150), and hydrophobic nano-silica BET:260 m^2/g/CB-SR (OCV-260)) were prepared, and OCV-260 effectively eliminated the shoulder peak effect in the Resistance-strain response signals. By reducing the polarity and hydrogen bond density through the hydrophobic groups on nano-silica (OB) surfaces, the spatial repulsion between CB and OB particles is maintained. This enables the formation of a continuous and reconfigurable conductive network within the silicone rubber (SR) matrix, preventing sudden resistance spikes during unloading. The formation and elimination mechanisms of the shoulder peak effect were elucidated through multiscale experiments and molecular dynamics (MD) simulations. OCV-260 showed a 78.84% reduction in the hysteresis area, a 97.19% increase in deformation sensitivity (GF), a 53.20% expansion in the monitoring range, and a response time of 221 ms. Its resistance response remained unaffected by the loading rate, and no shoulder effect was observed even after 1×10^4 cycles. These results demonstrate the broad application potential of CEC for flexible electronics, aerospace, and structural health monitoring. Furthermore, the molecular dynamics simulations in this study employed a simplified unitization model at the interfacial level, primarily aimed at revealing the trends and mechanisms of local interactions in the system evolution. However, they remain insufficient for directly characterizing the topological connectivity and cooperative restructuring processes of multi-filler conductive networks at the network scale. Future work may integrate multi-particle, coarse-grained simulations or mesoscopic statistical models to refine the description of network-scale behavior. Furthermore, incorporating DFT or quantum chemical methods to calculate the interaction energies and charge distributions of representative interface fragments can quantify the relative differences in hydrogen-bonded polar interactions under varying surface polarity conditions. This would provide a stronger mutual validation with the interface mechanism conclusions presented herein.

Conflict of Interests

The authors declare no interest conflict.

Electronic Supplementary Information

Electronic supplementary information (ESI) is available free of charge in the online version of this article at http://doi.org/10.1007/s10118-026-3609-6.

Data Availability Statement

The data that support the findings of this study are available from the corresponding author upon reasonable request.

ACKNOWLEDGMENTS

This work was financially supported by the National Natural Science Foundation of China (No 52368043).

REFERENCES

1 Zhang, Y.; Zhao, Y.; Qiu, M.; Hu, B.; Wang, B.; Wang, J.; Zheng, G.; Dai, K.; Jiang, Z.; Liu, C.; Shen, C. Interlocked architecture strategy for high-performance e-skin toward intelligent perception and photothermal-therapy. *Nano Energy* **2025**, *139*, 110912.
2 Zeng, J.; Jing, X.; Lin, L.; Wang, G.; Zhang, Y.; Feng, P. Smart sensing hydrogel actuators conferred by MXene gradient arrangement. *J. Colloid Interface Sci.* **2025**, *677*, 816–826.
3 Jeon, J. Y.; Kwon, S.; Ko, Y.; Jung, J.; Sung, B. J.; Kim, H. High-performance stretchable conductive composites for washable textile electronics via intermolecular interaction control. *Chem. Eng. J.* **2025**, *518*, 164488.
4 Chen, C.; Wang, P.; Hong, W.; Zhu, X.; Hao, J.; He, C.; Hou, H.; Kong, D.; Liu, T.; Zhao, Y.; Guo, X. Arch-inspired flexible dual-mode sensor with ultra-high linearity based on carbon nanomaterials/conducting polymer composites for bioelectronic monitoring and thermal perception. *Compos. Sci. Technol.* **2025**, *267*, 111182.
5 Yang, D.; Zhao, K.; Yang, R.; Zhou, S. W.; Chen, M.; Tian, H.; Qu, D. H. A rational design of bio-derived disulfide CANs for wearable

Graphical Abstract

Polarity-regulated Nano-Silica Steering Carbon Black Network Evolution and Reconfiguration in Conductive Silicone Elastomers: Experimental and Molecular Simulations

Bang-Wei Wan and Yang Yang

Kunming University of Science and Technology

Hydrogen-bond regulation *via* hydrophobic nano-silica suppresses shoulder peak effects, stabilizes conductive networks, and enables highly sensitive, wide-range, and durable resistive strain sensing in conductive elastomer composites.

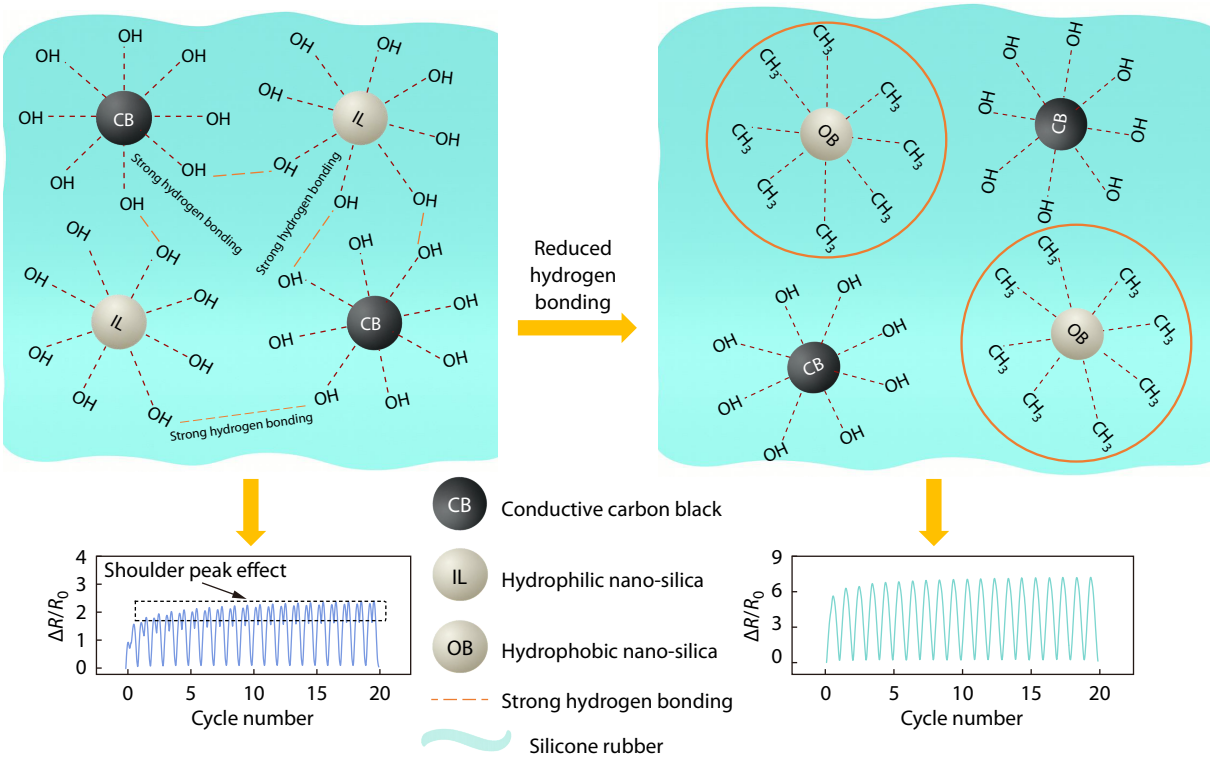

Chinese J. Polym. Sci. 2026, 44, 1883–1897 *https://doi.org/10.1007/s10118-026-3609-6*

capacitive pressure sensor. *Adv. Mater.* **2024**, *36*, 2403880.

6 Hong, W.; Guo, X.; Zhang, T.; Zhu, X.; Su, Z.; Meng, Y.; Zhao, Y.; Xu, D.; Pan, J.; Huang, Y.; Wang, H.; Xu, K.; Dong, H.; Zhang, C.; Li, Y.; Yan, X.; Huang, X. Dual bionic-inspired stretchable strain sensor based on graphene/multi-walled carbon nanotubes/polymer composites for electronic skin. *Compos. Part A: Appl. Sci. Manuf.* **2024**, *179*, 108043.

7 Hong, W.; Guo, X.; Li, X.; Zhang, T.; Zhu, X.; He, J.; Zhang, R.; Yang, S.; Shao, Y.; Fang, Y.; Yin, Z.; Sun, X.; Hu, J.; Hong, Q.; Zhao, Y. Fishbone and nettle fiber inspired stretchable strain sensor with high sensitivity and wide sensing range for wearable electronics. *Chem. Eng. J.* **2024**, *492*, 152281.

8 Yang, Z.; Zhang, S.; Chen, Z.; Lai, X.; Li, H.; Zeng, X. Self-healing and degradable polycaprolactone-based polyurethane elastomer for flexible stretchable strain sensors. *ACS Appl. Polym. Mater.* **2023**, *6*, 905−914.

9 Lu, Y.; Zhao, D.; He, J.; Zou, L. Armadillo-inspired ultra-sensitive flexible sensor for wearable electronics. *Chem. Eng. J.* **2023**, *475*, 146171.

10 Li, T.; Qi, H.; Dong, X.; Li, G.; Zhai, W. Highly robust conductive organo-hydrogels with powerful sensing capabilities under large mechanical stress. *Adv. Mater.* **2023**, *36*, 2304145.

11 Tang, J.; Wu, Y.; Ma, S.; Yan, T.; Pan, Z. Strain-sensing composite nanofiber filament and regulation mechanism of shoulder peaks based on carbon nanomaterial dispersion. *ACS Appl. Mater. Interfaces* **2023**, *15*, 7392−7404.

12 Cui, X.; Jiang, Y.; Xu, Z.; Xi, M.; Jiang, Y.; Song, P.; Zhao, Y.; Wang, H. Stretchable strain sensors with dentate groove structure for enhanced sensing recoverability. *Compos. Part B: Eng.* **2021**, *211*, 108641.

13 Jiang, Y.; Liu, Z.; Matsuhisa, N.; Qi, D.; Leow, W. R.; Yang, H.; Yu, J.; Chen, G.; Liu, Y.; Wan, C.; Liu, Z.; Chen, X. Auxetic mechanical metamaterials to enhance sensitivity of stretchable strain sensors. *Adv. Mater.* **2018**, *30*, 1706589.

14 Liu, X.; Wang, Y.; Li, R.; Yang, Y.; Niu, K.; Fan, Z.; Guo, R. Resistance sensing response optimization and interval loading continuity of multiwalled carbon nanotube/natural rubber composites: experiment and simulation. *J. Appl. Polym. Sci.* **2022**, *139*, e52430.
15 Gao, J. H.; Wan, B.; Zheng, M. S.; Luo, L.; Zhang, H.; Zhao, Q. L.; Chen, G.; Zha, J. W. High-toughness, extensile and self-healing PDMS elastomers constructed by decuple hydrogen bonding. *Mater. Horiz.* **2024**, *11*, 1305–1314.
16 Wu, J.; Zeng, F.; Fan, Z.; Xuan, S.; Hua, Z.; Liu, G. Hierarchical hydrogen bonds endow supramolecular polymers with high strength, toughness, and self-healing properties. *Adv. Funct. Mater.* **2024**, *34*, 2410518.
17 Liu, H.; Li, S.; Wang, M.; Liu, H.; Jiang, J.; Shao, S.; Wang, Z. Toughened polybenzoxazine coating matrix with improved comprehensive performance through hydrogen bond tuning with new polyurethanes. *Prog. Org. Coat.* **2023**, *180*, 107555.
18 Cui, J.; Zeng, F.; Wang, Y. A coarse-grained molecular dynamics study on the mechanical behavior of carbon nanotubes reinforced vulcanized natural rubber composites. *Polym. Compos.* **2023**, *44*, 7752–7767.
19 Yang, B.; Li, Y.; Wang, S.; Nie, R.; Wang, Q. Aminosilane modified graphene oxide for reinforcing nitrile butadiene rubber: experiments and molecular dynamic simulations. *Compos. Sci. Technol.* **2023**, *235*, 109956.
20 Rotaru, R.; Savin, M.; Tudorachi, N.; Peptu, C.; Samoila, P.; Sacarescu, L.; Harabagiu, V. Ferromagnetic iron oxide–cellulose nanocomposites prepared by ultrasonication. *Polym. Chem.* **2018**, *9*, 860–868.
21 Dilip, H. N.; Chakraborty, D. Hydrophilicity of the hydrophobic group: effect of cosolvents and ions. *J. Mol. Liq.* **2019**, *280*, 389–398.
22 Liu, X.; Liu, S.; Fan, M.; Zhang, L. Decrease of hydrophilicity of lignite using CTAB: effects of adsorption differences of surfactant onto mineral composition and functional groups. *Fuel* **2017**, *197*, 474–481.
23 Bao, W.; Liang, X.; Liu, Y.; Gao, Y.; Wang, J. Effects of AC and DC corona on the surface properties of silicone rubber: characterization by contact angle measurements and XPS high resolution scan. *IEEE Trans. Dielectr. Electr. Insul.* **2017**, *24*, 2911–2919.
24 Liu, W.; Jin, Y.; Tan, X.; Yeung, A. Altering the wettability of bitumen-treated glass surfaces with ionic surfactants. *Fuel* **2011**, *90*, 2858–2862.
25 Jiang, X.; Xu, M.; Wang, M.; Ma, Y.; Zhang, W.; Zhao, Y.; Ren, H.; Li, X. Preparation and molecular dynamics study of polyurethane damping elastomer containing dynamic disulfide bond and multiple hydrogen bond. *Eur. Polym. J.* **2022**, *162*, 110893.
26 Lewis, C. L.; Stewart, K.; Anthamatten, M. The influence of hydrogen bonding side-groups on viscoelastic behavior of linear and network polymers. *Macromolecules* **2014**, *47*, 729–740.
27 Zhang, B.; Dong, Y.; Han, J.; Zhen, Y.; Hu, C.; Liu, D. Physicochemical dual cross-linking conductive polymeric networks combining high strength and high toughness enable stable operation of silicon microparticle anodes. *Adv. Mater.* **2023**, *35*, e2301320.
28 Qiao, H.; Wu, B.; Sun, S.; Wu, P. Entropy-driven design of highly impact-stiffening supramolecular polymer networks with salt-bridge hydrogen bonds. *J. Am. Chem. Soc.* **2024**, *146*, 7533–7542.
29 Hu, Z.; Song, Z.; Huang, Z.; Tao, S.; Song, B.; Cao, Z.; Hu, X.; Wu, J.; Li, F.; Deng, W.; Hou, H.; Ji, X.; Zou, G. Reconstructing hydrogen bond network enables high voltage aqueous zinc-ion supercapacitors. *Angew. Chem. Int. Ed.* **2023**, *62*, e202309601.
30 Kim, E.; Kim, D.; Kwak, K.; Nagata, Y.; Bonn, M.; Cho, M. Wettability of graphene, water contact angle, and interfacial water structure. *Chem* **2022**, *8*, 1187–1200.
31 Xiao, J.; Zhang, Z.; Luan, Y.; Wu, S.; Wu, Y. Influence of carbon black surface characteristics on CB-NR interfacial interaction: molecular simulation and experimental study. *Compos. Part A: Appl. Sci. Manuf.* **2024**, *182*, 108198.
32 Huang, L.; Song, Z.; Song, X.; Yu, F.; Lu, A.; He, H.; Liu, W.; Wang, Z.; Zhang, P.; Li, S.; Zhao, X.; Cui, S.; Zhu, C.; Liu, Y. Performance enhancement of silicone rubber using superhydrophobic silica aerogel with robust nanonetwork structure and outstanding interfacial effect. *ACS Appl. Mater. Interfaces* **2024**, *16*, 22580–22592.
33 Sifri, R. J.; Padilla-Vélez, O.; Coates, G. W.; Fors, B. P. Controlling the shape of molecular weight distributions in coordination polymerization and its impact on physical properties. *J. Am. Chem. Soc.* **2019**, *142*, 1443–1448.
34 Zhang, N.; Shen, Z.; Chen, C.; He, G.; Hao, C. Effect of hydrogen bonding on self-diffusion in methanol/water liquid mixtures: a molecular dynamics simulation study. *J. Mol. Liq.* **2015**, *203*, 90–97.
35 Chen, Q.; Huang, W.; Zhang, L.; Chen, Y.; Liu, J. Impact of sacrificial hydrogen bonds on the structure and properties of rubber materials: insights from all-atom molecular dynamics simulations. *Langmuir* **2024**, *40*, 11470–11480.
36 Carbone, P.; Müller-Plathe, F. Molecular dynamics simulations of polyaminoamide (PAMAM) dendrimer aggregates: molecular shape, hydrogen bonds and local dynamics. *Soft Matter* **2009**, *5*, 2638–2647.
37 Qiao, B.; Zhao, X.; Yue, D.; Zhang, L.; Wu, S. A combined experiment and molecular dynamics simulation study of hydrogen bonds and free volume in nitrile-butadiene rubber/hindered phenol damping mixtures. *J. Mater. Chem.* **2012**, *22*, 12339–12348.
38 Zhou, B.; Liu, Z.; Li, C.; Li, L.; Zhang, X.; Sheng, Y.; Zhou, Y.; Jiang, L.; Tian, M.; Chen, S. Fabrication of ultrasensitive and flexible strain sensor based on multi-wall carbon nanotubes coated electrospun styrene-ethylene-butylene-styrene block copolymer fibrous tubes. *Eur. Polym. J.* **2022**, *178*, 111501.
39 Li, Z.; Qi, X.; Xu, L.; Lu, H.; Wang, W.; Jin, X.; Md, Z. I.; Zhu, Y.; Fu, Y.; Ni, Q.; Dong, Y. Self-repairing, large linear working range shape memory carbon nanotubes/ethylene vinyl acetate fiber strain sensor for human movement monitoring. *ACS Appl. Mater. Interfaces* **2020**, *12*, 42179–42192.
40 Zhao, S.; Li, Y.; Wu, F.; Hu, R.; Deng, C. Humidity response of single carbon nanocoil and its temperature sensor independent of humidity and strain. *Appl. Surf. Sci.* **2022**, *605*, 154745.
41 Wen, N.; Guan, X.; Fan, Z.; Guo, Y.; Cong, T.; Huang, H.; Li, C.; Zhang, J.; Lei, B.; Yang, R.; Liu, L.; Pan, L. A highly stretchable and breathable self-powered dual-parameter sensor for decoupled temperature and strain sensing. *Org. Electron.* **2023**, *113*, 106723.
42 Wang, H.; He, X.; Huang, X.; Su, P.; Xia, T.; Liu, W.; Ye, Y. Vapor-based fabrication of PEDOT coating for wearable strain sensors with excellent sensitivity and self-cleaning capability. *Mater. Today Chem.* **2023**, *28*, 101361.
43 Kim, S.; Yoo, B.; Miller, M.; Bowen, D.; Pines, D. J.; Daniels, K. M. EGaIn-silicone-based highly stretchable and flexible strain sensor for real-time two joint robotic motion monitoring. *Sens. Actuators A: Phys.* **2022**, *342*, 113659.

https://doi.org/10.1007/s10118-026-3609-6